H. Hasegawa[1,2], R. E. Denton[3], K. Dokgo[2], K.-J. Hwang[2], T. K. M. Nakamura[4], and J. L. Burch[2]

[1]Institute of Space and Astronautical Science, Japan Aerospace Exploration Agency, Sagamihara, Japan.

[2]Southwest Research Institute, San Antonio, TX, USA.

[3]Department of Physics and Astronomy, Dartmouth College, Hanover, NH, USA.

[4]Space Research Institute, Austrian Academy of Sciences, Graz, Austria.

Corresponding author: Hiroshi Hasegawa (`hasegawa.hiroshi@jaxa.jp`)

Key Points:

- Ion-scale magnetic flux rope (ISFR) can be generated from reconnecting electron-scale current sheet (ECS) at the subsolar magnetopause
- Preceding ion- to MHD-scale flux ropes had axial directions akin to that of the ISFR in the ECS, suggesting the same generation mechanism
- ISFR in the ECS had complex magnetic topology with three-dimensional effects and patchy, intense energy conversion in separatrix regions

Abstract

We present in-depth analysis of three southward-moving meso-scale (ion- to magnetohydrodynamic-scale) flux transfer events (FTEs) and subsequent crossing of a reconnecting electron-scale current sheet (ECS), which were observed on 8 December 2015 by the Magnetospheric Multiscale spacecraft near the subsolar magnetopause under southward and duskward magnetosheath magnetic field conditions. Our aims are to understand the generation mechanism of ion-scale magnetic flux ropes (ISFRs) and to reveal causal relationship among magnetic structures of the ECS, electromagnetic energy conversion, and kinetic processes in magnetic reconnection layers. Magnetic field reconstruction methods show that a flux rope with a length of about one ion inertial length existed and was growing in the ECS, supporting the idea that ISFRs can be generated from secondary magnetic reconnection in ECS. Grad-Shafranov reconstruction applied to the three FTEs shows that the FTE flux ropes had axial orientations similar to that of the ISFR in the ECS. This suggests that these FTEs also formed through the same secondary reconnection process, rather than multiple X-line reconnection at spatially separated locations. Four-spacecraft observations of electron pitch-angle distributions and energy conversion rate $\mathbf{j} \bullet \mathbf{E}^{'} = \mathbf{j} \bullet (\mathbf{E} + \mathbf{v}_e \times \mathbf{B})$ suggest that the ISFR had three-dimensional magnetic topology and secondary reconnection was patchy or bursty. Previously reported positive and negative values of $\mathbf{j} \bullet \mathbf{E}^{'}$, with magnitudes much larger than expected for typical magnetopause reconnection, were seen in both magnetosheath and magnetospheric separatrix regions of the ISFR. Many of them coexisted with bi-directional electron

beams and intense electric field fluctuations around the electron gyrofrequency, consistent with their origin in separatrix activities.

Plain Language Summary

Magnetic reconnection is a physical process that converts magnetic energy into plasma energy by changing the connectivity of magnetic field lines from one region to another. Magnetic reconnection at the outer boundary of planetary magnetospheres, known as the magnetopause, is key to the entry of solar wind plasma and energy into the magnetospheres that forms the basis for space weather phenomena in the magnetospheres. Magnetopause reconnection often occurs in a transient or patchy manner, forming magnetic flux ropes with helical field lines of various sizes. They may become an important pathway for fast coupling between the solar wind and magnetosphere. However, the generation mechanism of a subclass of flux ropes, relatively small "ion-scale" flux ropes, is poorly understood. Computer simulations show that they are formed in thin and elongated current sheets of single active reconnection site, but this scenario has not been confirmed by observations. Our observations based on NASA's Magnetospheric Multiscale mission show that ion-scale flux rope can form in a thin current sheet of single ongoing reconnection site at Earth's magnetopause. The observed flux rope showed signatures of complex field line connectivity and localized conversion from electromagnetic to electron energy and vice versa, indicating complex magnetopause dynamics.

1 Introduction

Magnetopause reconnection often occurs in a time-dependent and/or localized manner, generating flux transfer events (FTEs). FTEs are characterized by a bipolar variation of the magnetic field component normal to the nominal magnetopause and also generally by an enhancement of the field magnitude around the event center (see Raeder (2006) and Hasegawa (2012) for reviews). While large-scale FTEs (typically with dimensions ~1 R_E) have been extensively investigated both theoretically and observationally and their formation processes are relatively well known (e.g., Fear et al., 2012), little is known about the generation mechanism of ion-scale FTEs or magnetic flux ropes (FRs) with sizes comparable to or somewhat larger than ion inertial length (typically ~50 km at the dayside magnetopause). They have been observed in exhaust regions of both magnetopause (Eastwood et al., 2016) and magnetotail (Stawarz et al., 2018) reconnection.

Numerical simulations of magnetic reconnection show that ion-scale FRs can form through secondary magnetic reconnection in an elongated portion of reconnecting current sheets with electron-scale thicknesses. Two-dimensional kinetic simulations show that secondary reconnection can occur regardless of the presence (Drake et al., 2006) or absence (Hesse et al., 1999; Daughton et al., 2006) of guide field, the magnetic field component in the direction of X-line. Dong et al. (2017) reported observations by the Magnetospheric Multiscale (MMS) spacecraft (Burch et al., 2016) of three consecutive FTEs, which were followed by an

encounter of reconnecting electron-scale current sheet (ECS) (Burch & Phan, 2016), and suggested that these FTEs formed through secondary reconnection in the ECS. Recently, Hasegawa et al. (2022) demonstrated that electron-scale magnetic islands (FRs in the absence of guide field) can form and grow in an electron-scale current sheet of magnetotail reconnection. Although these observations (Eastwood et al., 2016; Dong et al., 2017; Hasegawa et al., 2022) are consistent with the secondary reconnection scenario, there is a gap in our understanding about the link between electron-scale FRs in reconnecting ECS and ion-scale FRs in large-scale reconnection jets or exhausts; can electron-scale FRs grow to form ion-scale FRs? This question needs attention because electron-scale FRs may be dissipated in reconnecting ECS through magnetic field annihilation, which was recently confirmed in simulations by Nakamura et al. (2021) and observations by Hasegawa et al. (2022).

Another interesting feature of ECSs reconnecting at the magnetopause is that the energy conversion rate $\mathbf{j}\bullet\mathbf{E}^{'} = \mathbf{j}\bullet(\mathbf{E}+\mathbf{v}_e\times\mathbf{B})$ (Zenitani et al., 2011) observed in or around magnetopause electron diffusion regions (EDRs) often exceeds the values ($\leq 4\ nW/m^3$) expected for typical magnetopause reconnection (Webster et al., 2018). What is peculiar is that $\mathbf{j}\bullet\mathbf{E}^{'}$ often exhibits oscillatory or bipolar features, with both positive and negative values (Genestreti et al., 2017; Burch et al., 2018). Genestreti et al. (2022) discussed possible causes of these intense and oscillatory energy conversion signatures and effects of upstream (magnetosheath) and boundary conditions. However, since the reconnection region geometry and spacecraft path with respect to reconnection layer structures are often hardly known from in-situ measurements, their origins are not fully understood.

In the present study, we revisit MMS observations of magnetopause FTEs and ECS on 8 December 2015, reported by Dong et al. (2017) and Burch and Phan (2016), respectively. The ECS in this event showed multiple oscillatory $\mathbf{j}\bullet\mathbf{E}^{'}$ features (Burch et al., 2018), and thus the event is ideal for investigating both the FTE generation process and origin of anomalous energy conversion in ECS. The structures of the FTEs and ECS are recovered by Grad-Shafranov reconstruction (GSR) and electron magnetohydrodynamics (EMHD) reconstruction methods, respectively. Our intents are to reveal not only the generation mechanism of ion-scale flux ropes but also the interrelationship among the magnetic field structure, oscillatory $\mathbf{j}\bullet\mathbf{E}^{'}$, and kinetic processes responsible for energy conversion in the ECS.

The outline of the present paper is as follows. In section 2, an overview is given of MMS observations surrounding the magnetopause ECS on 8 December 2015. In section 3, results from both the GSR and EMHD reconstruction are presented and discussed. In section 4, detailed discussions are given about three-dimensional aspects of the ECS, origins of the oscillatory $\mathbf{j}\bullet\mathbf{E}^{'}$, and formation and decay processes of FTEs. A brief summary is presented in section 5.

2 Event Overview and Data

Figure 1 shows an overview of observations by the MMS3 spacecraft near the

subsolar magnetopause of three FTEs or FRs, reported by Dong et al. (2017), and an electron-scale current sheet (ECS), reported by Burch and Phan (2016) and Burch et al. (2018), on 8 December 2015, 11:19:35–11:21:05 UT. MMS was located at (10.2, 1.3, –1.4) R_E in GSM. Since near the subsolar point the normal direction of the nominal magnetopause is roughly along the x_{GSM} axis, B_x can be taken as the normal field component. For each of the three FRs, negative to positive B_x variation as a typical signature of southward moving FTEs is clearly seen during the interval sandwiched between the dashed black vertical lines (Figure 1a). Consistently, southward reconnection ion jets were observed, in particular, during trailing parts of the FR2 and FR3 intervals (Figure 1b). A density enhancement, likely caused by compression on the leading side of FRs, was observed immediately before FR3 (Figure 2d). In the present event, the static pressure in the magnetosheath (observed during an earlier part of the interval) was dominated by ion thermal pressure. A peak in the static pressure as another typical signature of FTEs was clearly seen at or near the center of all three FRs (Figure 1g). The pressure increase was due to an enhancement of the core magnetic field component, which was roughly B_y in the present case (Figure 1a).

Following these three FTEs, MMS crossed an electron-scale magnetopause current sheet at 11:20:43 UT, as indicated by high-speed electron flows predominantly in the $-y_{\mathrm{GSM}}$ direction (Figure 1c), from the magnetosheath into the magnetosphere. The electron temperature strongly increased during this crossing, especially in the direction parallel to the magnetic field (Figure 1f). Possible electron heating processes are discussed in section 4.2. This current sheet was interpreted to be of an electron diffusion region (EDR) by Burch and Phan (2016), but we will show in sections 3.2 and 4 that it involved complex magnetic structures and energy conversion processes not close to X-line(s) but in separatrix regions.

MMS data used in the present study are magnetic fields from the fluxgate magnetometers (FGM) (Russell et al., 2016), electric fields from the double-probe instruments (Ergun et al., 2016; Lindqvist et al., 2016), and ion and electron moments and electron velocity distributions from the Fast Plasma Investigation instrument suite (FPI) (Pollock et al., 2016).

3 Reconstruction of Magnetic Flux Ropes and Magnetopause Current Sheet

In order to gain insights into the generation process of the observed FTEs or FRs, we reconstruct magnetic structures of the three FRs and electron-scale current sheet at the magnetopause from MMS data. Grad-Shafranov reconstruction for recovering two-dimensional (2D) magnetohydrostatic structures (Hau and Sonnerup, 1999; Sonnerup et al., 2006) is applied to the three FRs. A method for recovering 2D sub-ion-scale reconnection regions, known as the EMHD reconstruction (Sonnerup et al., 2016; Hasegawa et al., 2021), and polynomial reconstruction technique for three-dimensional (3D) magnetic field structures (Torbert et al., 2020; Denton et al., 2020; Denton et al., 2022) are used to analyze the ECS.

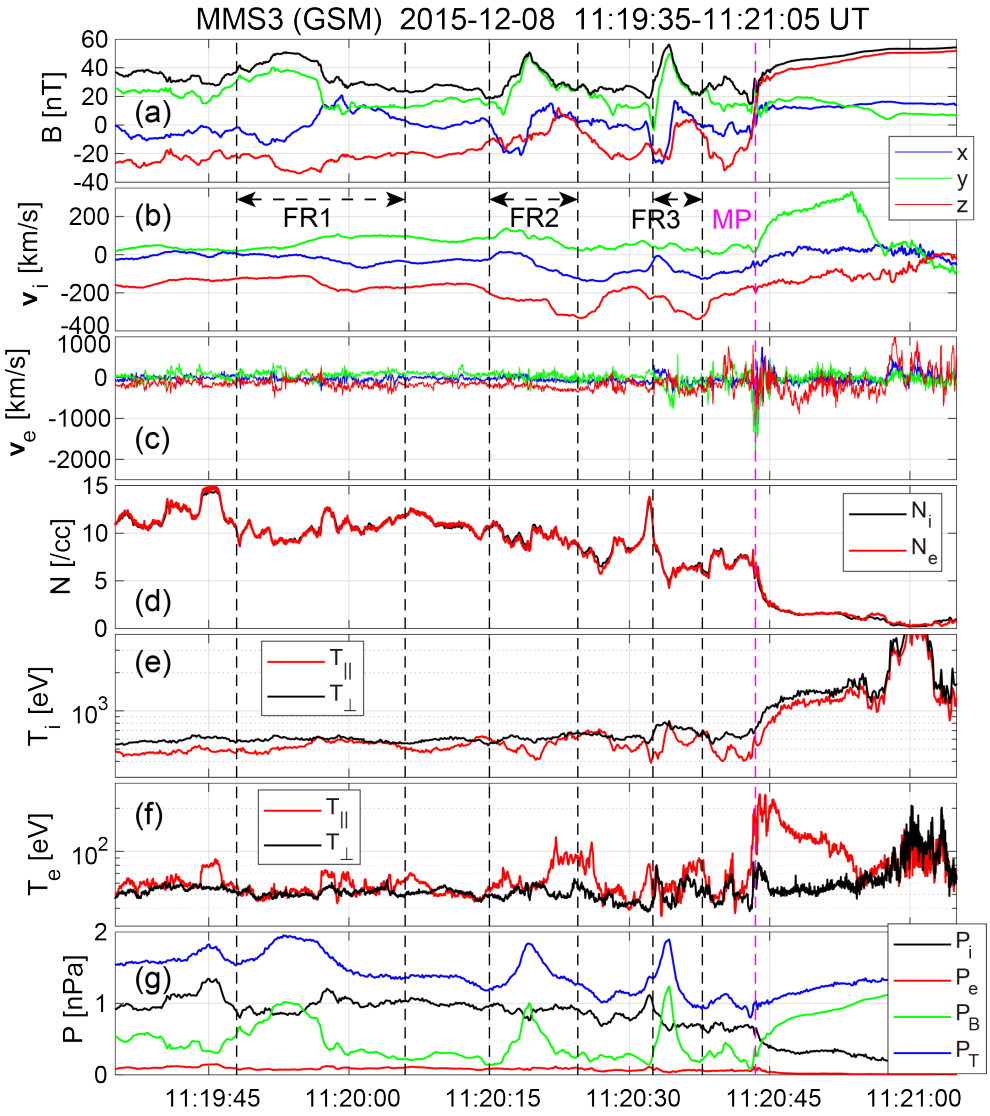

Figure 1. Burst-mode data during three flux transfer events (FTEs) and magnetopause (MP) current sheet crossing recorded by the MMS3 spacecraft on 8 December 2015. Three FTEs were interpreted as being magnetic flux ropes (FRs) by Dong et al. (2017) and are called as such in the present paper. (**a**) Magnetic field in geocentric solar magnetospheric (GSM) coordinates, (**b**) ion velocity at 150 ms resolution, (**c**) electron velocity at 30 ms resolution, (**d**) ion and electron densities, (**e**) ion temperatures in the directions parallel and perpendicular to the magnetic field, (**f**) parallel and perpendicular temperatures of electrons, and (**g**) ion, electron, magnetic, and total pressures. Three sets of vertical black dashed lines indicate the time intervals used for the Grad-Shafranov

reconstruction. All figures except for Figure 7 of the present paper were created by Matlab (see Data Availability Statement of Hasegawa et al. (2021)).

3.1 Grad-Shafranov reconstruction

Grad-Shafranov reconstruction (GSR) is a single-spacecraft method for the reconstruction of 2D magnetic field structures on the MHD scale from magnetic field and plasma pressure data. It allows for the production of 2D field maps in a region around the path of an observing spacecraft, and an estimation of the orientation of FR or invariant axis $\hat{\mathbf{z}}_{\rm GSR}$ along which spatial gradients are assumed to be negligibly small (Hu and Sonnerup, 2002). In addition to the 2D assumption, the magnetohydrostatic force balance is assumed; inertia terms in the MHD momentum equation can be neglected and thus the force from gradient of the total static pressure is approximately balanced with magnetic tension. The reconstruction is performed in a moving frame in which the structure looks approximately stationary, which is the deHoffmann-Teller (HT) frame (Khrabrov & Sonnerup, 1998) in the GSR case. The reconstruction coordinate system is defined as follows; $\hat{\mathbf{x}}_{\rm GSR}$ is antiparallel to the projection of the HT velocity $\mathbf{V}_{\rm HT}$ onto the plane perpendicular to $\hat{\mathbf{z}}_{\rm GSR}$, and $\hat{\mathbf{y}}_{\rm GSR} = \hat{\mathbf{z}}_{\rm GSR} \times \hat{\mathbf{x}}_{\rm GSR}$ forms the right-handed orthogonal system. In this coordinate system, the spacecraft is seen to move in time along the $\hat{\mathbf{x}}_{\rm GSR}$ axis in the reconstruction plane and at an axial velocity $-\mathbf{V}_{\rm HT} \bullet \hat{\mathbf{z}}_{\rm GSR}$.

Figure 2 shows 2D maps of the magnetic field and plasma pressure from the GSR method applied to MMS3 data for the three FRs. The spacecraft separation ~15 km was small on the MHD scale, so that the use of different spacecraft makes no significant difference. Table 1 shows parameters used in or obtained from the reconstruction. The HT analysis was applied to combined ion velocity and magnetic field data with 150 ms resolution. For all three FRs, the HT velocity is dominantly southward, with a duskward component. This is consistent with southward motion of the FTEs and the direction of reconnection jets expected on the southern side of dayside X-line under continuously southward and duskward magnetosheath field conditions (Figure 1a). The Walén relation (Paschmann & Sonnerup, 2008) is weakly satisfied, with its slope magnitude not close to unity; inertia effects were only modestly important in the MHD force balance. On the other hand, the negative slopes are consistent with the three FRs having been resided in or near reconnection exhausts on the southern side of the X-line(s) that generated these FRs.

For all three FTEs, the field maps show a flux rope structure with an intense core field component $B_{z\rm GSR}$ comparable to 50 nT. The flux rope lengths were roughly 1000 km, which was ~$14d_i$ with ion inertial length in the magnetosheath $d_i \sim 70$ km; all three FRs were of MHD scale, but much smaller than typical FTEs with sizes ~1 R_E (Hasegawa et al., 2006, 2010). The invariant axis was roughly oriented in the $y_{\rm GSM}$ direction, which was roughly the X-line orientation expected for the present external field conditions.

The in-plane flux content, defined as the amount of in-plane magnetic flux em-

bedded inside the red field lines in Figures 2a, 2c, and 2e is of order 5×10^{-3} Tesla • meter. This is roughly one order of magnitude smaller than the flux content for typical FTEs (Hasegawa et al., 2006). For the Alfvén speed ~150 km/s based on the reconnecting magnetic field component ~20 nT and density ~8 cm^{-3} (Figures 3a and 3e), the reconnection electric field expected for the dimensionless reconnection rate 0.1-0.2 (Liu et al., 2017) is 0.3-0.6 mV/m. Assuming that this reconnection electric field was sustained during the present event, the in-plane flux reconnected per 20 s, which was roughly the interval between two neighboring FRs in the present event (Figure 1), is 6×10^{-3} to 1.2×10^{-2} Tesla • meter. This value is comparable to the flux content of the three FRs (Table 1), which suggests that magnetic reconnection was continuously active at the X-line that produced the FRs and the corresponding reconnection region kept generating FRs.

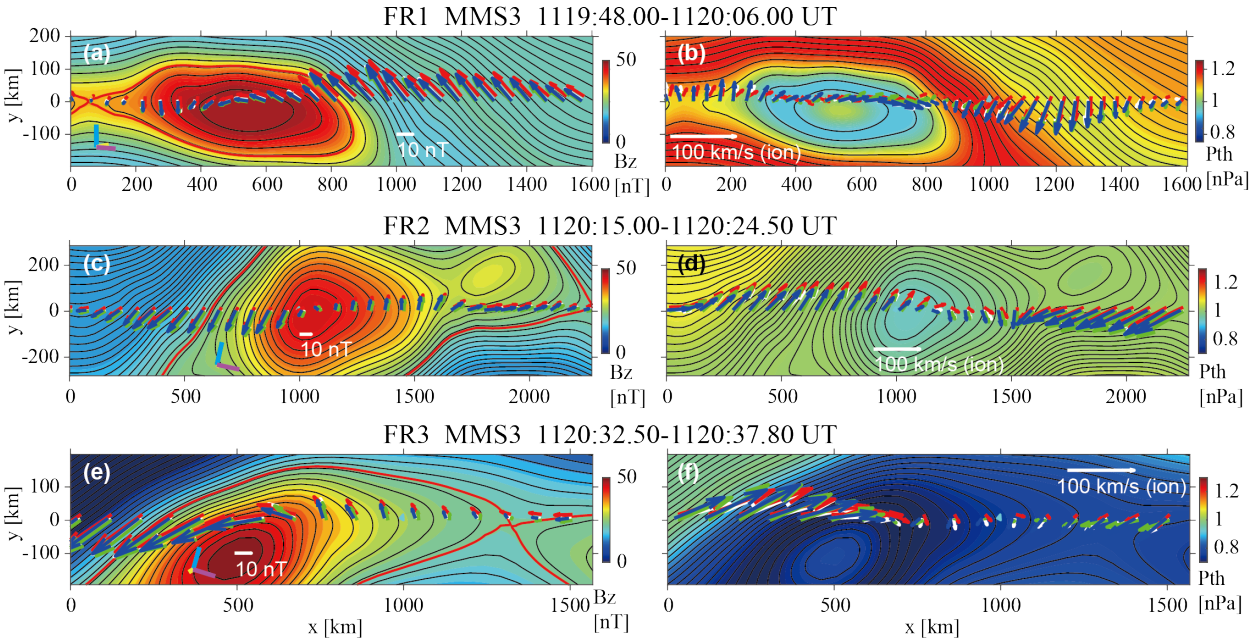

Figure 2. Two-dimensional (2-D) magnetic fields and pressures for the three FRs (FR1, FR2, and FR3), reconstructed from MMS3 data by use of the Grad-Shafranov reconstruction (GSR) method. Black curves show the reconstructed in-plane magnetic field lines, with the axial component B_z in color in panels (**a, c, e**) and plasma thermal pressure in color in panels (**b, d, f**). The white, red, green, and blue arrows in panels (**a, c, e**) are the projections onto the reconstruction (x-y) plane of the magnetic fields measured by MMS1, MMS2, MMS3, and MMS4, respectively, and those in panels (**b, d, f**) are the measured ion velocities transformed into the deHoffmann-Teller frame. The cyan, yellow, and magenta bars near the lower-left corner of panels (**a, c, e**) are the projections of the unit vectors of the GSM x, y, and z axes, respectively. The in-plane flux

contents inside the FRs bounded by the red curve in Figures 2a, 2c, and 2e are shown in Table 1.

3.2 Reconstruction of the electron-scale magnetopause current sheet

The EMHD reconstruction is a single-spacecraft method for the reconstruction of 2D electromagnetic and electron velocity fields in and around the EDRs of magnetic reconnection from magnetic field, electric field, and electron moment data (Sonnerup et al., 2016). It is based on a 2D and time-independent form of the electron MHD equations assuming isotropy for the diagonal components of the electron pressure tensor. The most recent version allows for incorporating the effects of electron inertia, nonuniform electron density and temperature, and guide magnetic field (Hasegawa et al., 2021). A first trial reconstruction is usually performed in a structure-rest frame estimated by the Spatio-Temporal Difference (STD) method (Shi et al., 2019) and using an invariant axis ($\hat{\mathbf{z}}_{\mathrm{EMHD}}$) orientation or $\mathbf{M}$ direction estimated by a hybrid method (Denton et al., 2018). The hybrid method is based on combined use of the minimum variance analysis of the magnetic field and Maximum Directional Derivative method (Shi et al., 2019) applied to four-spacecraft measurements of the magnetic field (MDDB). EMHD reconstruction coordinates are defined in a similar manner to the GSR method. The final frame velocity $\mathbf{V}_{\mathrm{str}}$ and coordinate system used for optimized reconstruction results are determined by a trial-and-error method (Hasegawa et al., 2017). It attempts to maximize the correlation coefficient between the normalized components of the measured magnetic field and electron velocity and those predicted from the reconstructed field maps along the paths of the three spacecraft not used as input for the reconstruction.

Table 1. Results summarizing the Grad-Shafranov reconstruction applied to three magnetic flux ropes (FRs).

	FR1	FR2	FR3
Time interval (UT)	1119:48.0 – 1120:06.0	1120:15.0 – 1120:24.5	1120:32.5 – 1
$\mathbf{V}_{\mathrm{HT}}{}^{a}$ (km/s in GSM)	(–23.5, 112.3, –178.7)	(–39.2, 195.2, –265.0)	(–75.5, 101.4
Walen slope[b]	–0.234	–0.454	–0.205
Invariant axis $\hat{\mathbf{z}}$ (GSM)	(–0.1245, 0.8352, –0.5356)	(0.0559, 0.9884, –0.1412)	(0.1634, 0.97
$\hat{\mathbf{x}}$ (GSM)	(–0.0052, 0.5393, 0.8421)	(0.2163, 0.1261, 0.9682)	(0.2693, –0.1
$\hat{\mathbf{y}}$ (GSM)	(0.9922, 0.1077, –0.0628)	(0.9747, –0.0846, –0.2067)	(0.9491, –0.1
In-plane flux content ($Tesla \bullet meter$)	2.0×10^{-3}	6.5×10^{-3}	6.0×10^{-3}
$\mathrm{CC}_B{}^{c}$	0.9967	0.9966	0.9941
θ^d (degree)	59.0	32.7	15.3

[a]$\mathbf{V}_{\mathrm{HT}}$: deHoffmann-Teller (HT) velocity (Khrabrov & Sonnerup, 1998). [b]Walén slope: slope of the regression line in a scatter plot of the components of ion velocities measured in the HT frame and those of the local Alfvén velocities during the interval (Paschmann & Sonnerup, 2008). [c]CC_B: the correlation coefficient between the GSM components of the magnetic field measured by,

and those predicted from the GSR map along the paths of, the three MMS spacecraft not used in the reconstruction. $^{\mathrm{d}}\theta$: angle between the flux rope axis and that of the ion-scale flux rope in the electron-scale current sheet observed at 1120:43 UT (Figure 4).

For the EMHD reconstruction, we use magnetic field, electric field, and electron moment data at 7.5 ms resolution (Rager et al., 2018), rather than 30 ms resolution of level-2 burst mode. The aim is to reveal fine scale structures in the current sheet of energy conversion and electron temperature which may have implications for kinetic and electron energization processes underlying energy conversion. Figure 3 shows the data from all four MMS spacecraft for 11:20:42.0–11:20:45.5 UT surrounding the reconstructed intervals. LMN coordinates in Figure 3 are the final ones used in the reconstruction: $\mathbf{L}_{\mathrm{EMHD}} = (0.3089,\ -0.4365,\ 0.8468)$, $\mathbf{M}_{\mathrm{EMHD}} = (-0.1692,\ -0.8995,\ -0.4029)$, and $\mathbf{N}_{\mathrm{EMHD}} = (0.9376,\ -0.0209,\ -0.3472)$ in GSM.

The current density was intense (Figure 3d) and comparable to those seen in EDRs reported in the literature (Burch et al., 2016; Webster et al., 2018). The B_N component shows substantial variations (Figure 3c) and the current density component j_M appears to be not single-peaked (Figure 3d), suggesting complex structures in the ECS. However, the MDDB analysis shows that the intermediate eigenvalue (equivalent to squared magnetic gradient in local $\mathbf{L}$) is much larger than the minimum eigenvalue (squared magnetic gradient in local $\mathbf{M}$) around the ECS center (Figure S1 in Supporting Information). This suggests that the local magnetic structure was approximately 2D, permitting the use of the EMHD method. On the other hand, the data variations in Figure 3 appear very different among the four spacecraft, in particular for B_M, B_N, and v_{eM}, during the ECS crossing. Provided the fact that the spacecraft separation ~15 km was comparable to the thickness of the ECS (Figure 4a), this suggests that the four spacecraft saw different portions of the ECS structure and/or different phases of ECS evolution.

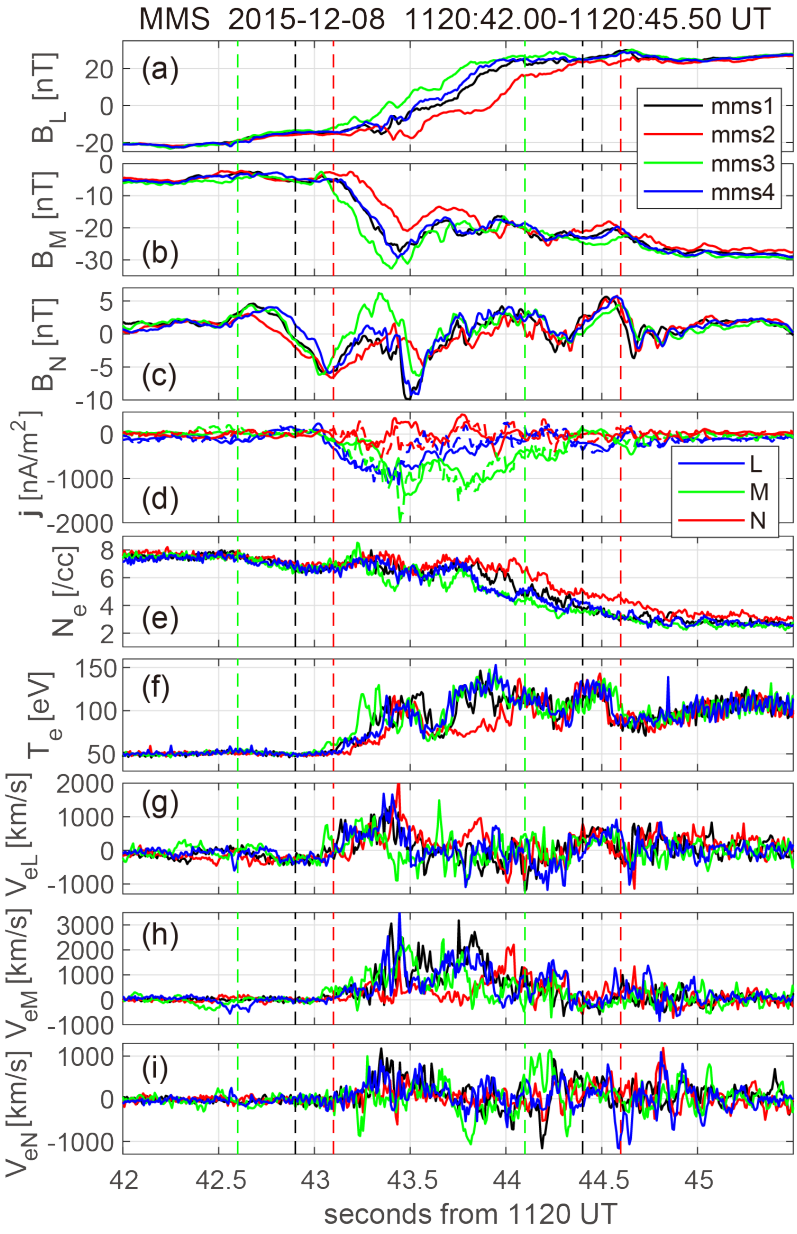

Figure 3. Data at 7.5 ms resolution from the four MMS spacecraft for the electron-scale magnetopause current sheet at 11:20 UT. (**a-c**) LMN components of the magnetic field, (**d**) current density at the MMS centroid from particle measurements (solid) and $\frac{(\nabla \times \mathbf{B})}{\mu_0}$ (dashed), (**e**) electron density, (**f**) electron temperature assuming isotropy, and (**g-i**) electron velocity. The LMN axes are estimated from optimization of the electron MHD (EMHD) reconstruction

results (see text for details). The intervals sandwiched between pairs of black, red, green, and blue vertical dashed lines are used for the EMHD reconstruction from MMS1, MMS2, MMS3, and MMS4 data, respectively (the intervals for MMS1 and MMS4 are the same and thus the blue lines are not seen).

Figure 4 shows field maps recovered from the up-to-date version of the EMHD reconstruction using MMS4 data. The structure velocity is $\mathbf{V}_{\rm str} = (-7.0,\ 15.7,\ -132.7)$ km s^{-1} in GSM, which is not extremely different from the average ion velocity during the interval $\langle \mathbf{V}_i \rangle = (-42.8,\ 38.9,\ -172.1)$ km s^{-1} (the L and N components of $\mathbf{V}_{\rm str}$ were optimized by the trial-and-error method, but its M component was taken to be that of $\langle \mathbf{V}_i \rangle$). GSM components of the reconstruction axes are: $\hat{\mathbf{x}}_{\rm EMHD} = (-0.0012,\ -0.4086,\ 0.9127)$, $\hat{\mathbf{y}}_{\rm EMHD} = (0.9856,\ -0.1549,\ -0.0681)$, and $\hat{\mathbf{z}}_{\rm EMHD} = (0.1692,\ 0.8995,\ 0.4029) = -\mathbf{M}_{\rm EMHD}$. The thickness of the reconstructed current sheet is not much larger than electron inertial length $d_e \sim 2.2$ km, but the ECS contains a magnetic flux rope with a length ~100 km, comparable to d_i (Figure 4a). Thus, this flux rope is hereafter referred to as the ion-scale flux rope (ISFR). The out-of-plane field component B_z has a peak not at the ISFR center but on the southern (lower-left in the map) side of the ISFR center (Figure 4b). This might be associated with 3D effects, as will be discussed in section 4.1. For each (magnetosheath or magnetospheric) side of the ECS, the electron density and temperature are assumed to be preserved along the in-plane field lines (Hasegawa et al., 2021). Thus, the reconstructed density shows abrupt jumps at the ECS center on some field lines (Figure 4c), because separate branches of the function $n_e(A)$ are used on the two sides and the branch is switched by the polarity of B_L (see Hu & Sonnerup (2003) for similar approach).

The reconnection electric field E_{z0}, which is optimized and assumed to be constant in the EMHD reconstruction, is 1.0 mV/m, which is comparable to 0.3 mV/m expected for the dimensionless reconnection rate 0.1 in the present case and those estimated for previously reported magnetopause EDR events (Burch et al., 2020; Hasegawa et al., 2017). However, we show in sections 3.3, 4.1, and 4.2 that the present ECS probably involved 3D dynamics and time-dependent or localized energy conversion processes; the measured electric field component $E_{z\rm EMHD}$ was not stable at all.

Figures 5a and 5b show scatter plots of the GSE components of the magnetic field and electron velocity in the structure frame, respectively, predicted from the MMS4 maps (Figure 4) versus those measured, along the MMS1, MMS2, and MMS3 paths. The correlation coefficient for the magnetic field $\mathrm{cc}_B = 0.9755$ is high, despite the fact that different spacecraft traversed different portions of the ECS and the structure appears to have been evolving, as will be discussed in section 3.3. This indicates that the reconstructed magnetic field (Figure 4a) represents some real features. On the other hand, the correlation coefficient for the electron velocity $\mathrm{cc}_V = 0.5924$ is much lower than cc_B. This is probably because errors in the reconstruction of electron streamlines are generally much

larger than for the in-plane magnetic field (Hasegawa et al., 2021) and the velocity structure was more 3D than the magnetic field. Indeed, while MMS1 and MMS4 traversed nearly the same portion of the 2D field (Figure 4a) and the measured magnetic field patterns are very similar for MMS1 and MMS4 (Figures 3a-3c), consistent with 2D magnetic field, the electron velocities measured by MMS1 and MMS4 have different directions in substantial portions of the interval (Figures 3g-3i and 4b). Considering that MMS1 and MMS4 were separated by 14.2 km ($\sim 6d_e$) in the out-of-plane (z_{EMHD}) direction (Table S1 in Supporting Information), this indicates that the velocity field had significant 3D structures of electron scale.

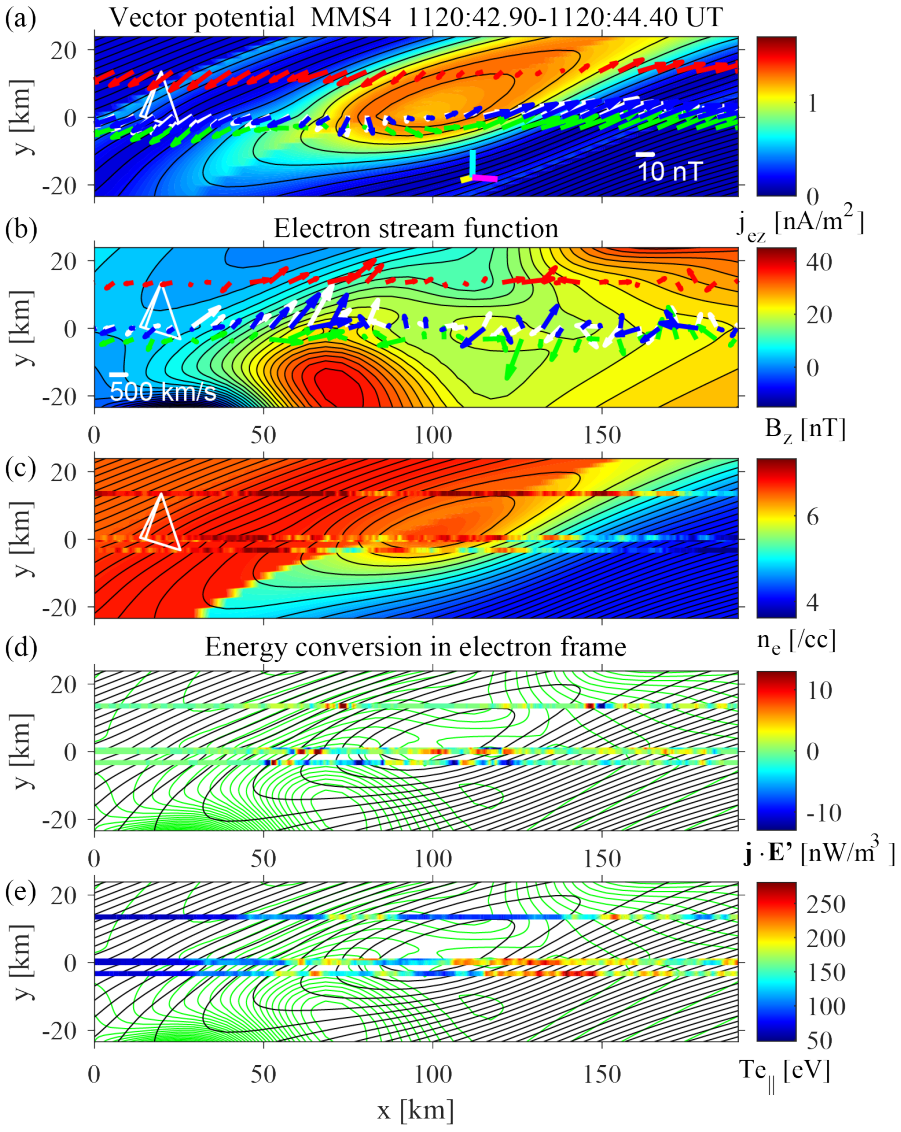

Figure 4. Field maps from the EMHD reconstruction method with electron inertia and compressibility effects (Hasegawa et al., 2021) applied to MMS4 data with 7.5 ms resolution. (**a**) Reconstructed in-plane magnetic field, with the recovered out-of-plane current density in color. (**b**) Reconstructed electron streamlines with the reconstructed out-of-plane magnetic field component in color. (**c**) Reconstructed electron density, with electron densities measured along the paths of the four spacecraft in color. (**d,e**) In-plane field lines (black) and electron streamlines (green), with measured electron-frame energy conversion rates $\mathbf{j} \bullet \mathbf{E}' = \mathbf{j} \bullet (\mathbf{E}+\mathbf{v}_e \times \mathbf{B})$ (Zenitani et al., 2011) (**d**) and parallel electron temperatures (**e**) in color. The white, red, green, and blue arrows in Figure 4a are the projections onto the reconstruction (x-y) plane of the magnetic fields measured by MMS1, MMS2, MMS3, and MMS4, respectively, while those Figure 4b are the measured electron velocities in the structure-rest frame. The cyan, yellow, and magenta bars in Figure 4a are the projections of the unit vectors of the GSM x, y, and z axes, respectively. In Figures 4c-4e, the MMS4 paths colored by the measured electron density, energy conversion rate, and electron temperature, respectively, are nearly on top of the MMS1 paths.

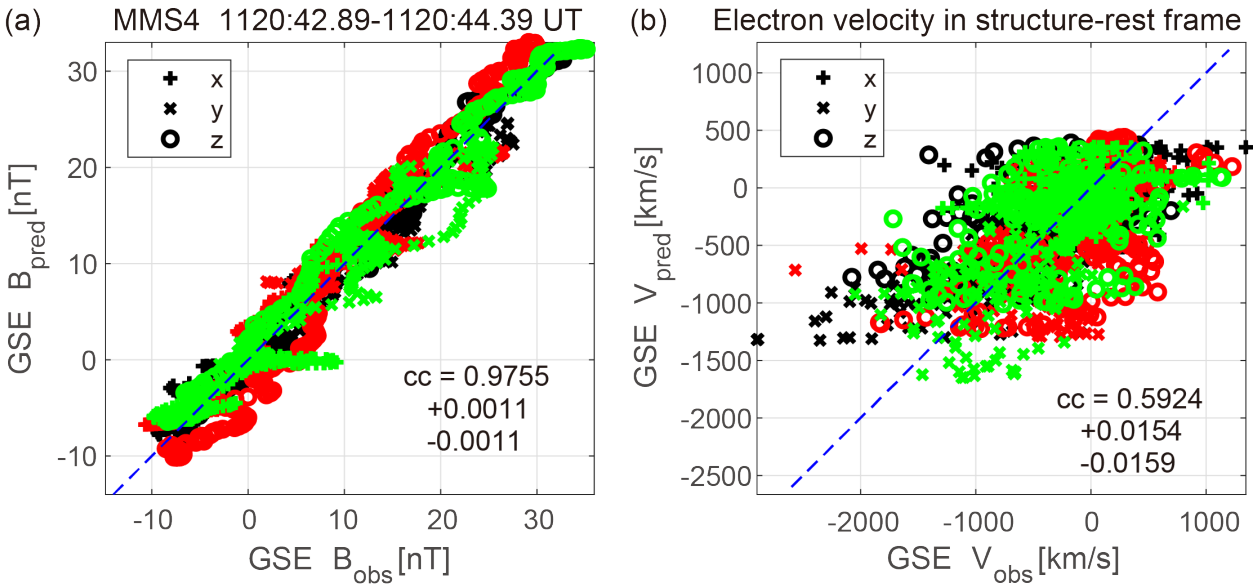

Figure 5. Correlations between the quantities predicted from the EMHD field maps (Figure 4) and those measured along the paths of the three spacecraft (MMS1, MMS2, and MMS3) not used in the reconstruction. GSM components of (**a**) the predicted versus measured magnetic fields, and (**b**) predicted versus measured electron velocities in the structure-rest frame.

3.3 Evolution of the electron-scale magnetopause current sheet

Figure 6 shows 2D magnetic field maps from all four spacecraft, plotted in the order of ECS crossing (Figure 3a) and using the same frame velocity and

coordinate system as for Figure 4. While the reconstructed field structure is similar for MMS4 and MMS1 which crossed the ECS nearly at the same time, those for MMS2 and MMS3 are distinct from those for the other two. We argue that this difference is due to time evolution of the structure, rather than structures in the z_{EMHD} direction. Note that MMS2 and MMS3 were located at a similar z_{EMHD} position between MMS1 and MMS4 (Table S1). If the difference was due to 3D effects, MMS2 and MMS3 at similar z_{EMHD} may have seen similar patterns in the field variations and MMS1 and MMS4 at largest (14.2 km) separation in z_{EMHD} may have seen rather different patterns. On the contrary, MMS1 and MMS4 saw similar magnetic field variations and MM2 and MMS3 saw quite different variation patterns (Figures 3a-3c). It thus seems fair to conclude that there was a significant time evolution of the ECS during a 0.5-sec period of the ECS crossing (Figure 3a), which is much longer than electron gyroperiod (1.4×10^{-3} s) and somewhat shorter than proton gyroperiod (2.5 s).

Figure 6 suggests that at the time when MMS3 crossed the ECS, a small (sub-ion-scale) flux rope existed (Figure 6a), it grew to become an ion-scale flux rope when MMS4 and MMS1 crossed the ECS (Figures 6b and 6c), and it was swept toward the north (right side in the map) in the reconstruction frame by the time MMS2 crossed the ECS (Figure 6d). Note, however, that the flux rope actually traveled southward in the spacecraft (or Earth's rest) frame, as is evident from the negative-then-positive B_N (Figure 3c). Figure S2 (in Supporting Information) shows 3D magnetic field lines in the L-N plane reconstructed for each moment in time from the polynomial reconstruction (Denton et al., 2022), using the four-spacecraft measurements of the magnetic field and current density from multiple times. Although a sequence of flux rope evolution appears different from that inferred from the EMHD reconstruction (Figure 6), they also suggest that an ion-scale or sub-ion-scale flux rope existed in the ECS when the MMS tetrahedron was near the center of the ECS. In summary, both the EMHD and polynomial reconstructions suggest that the ion-scale flux rope was generated from the electron-scale current sheet reconnecting at the magnetopause.

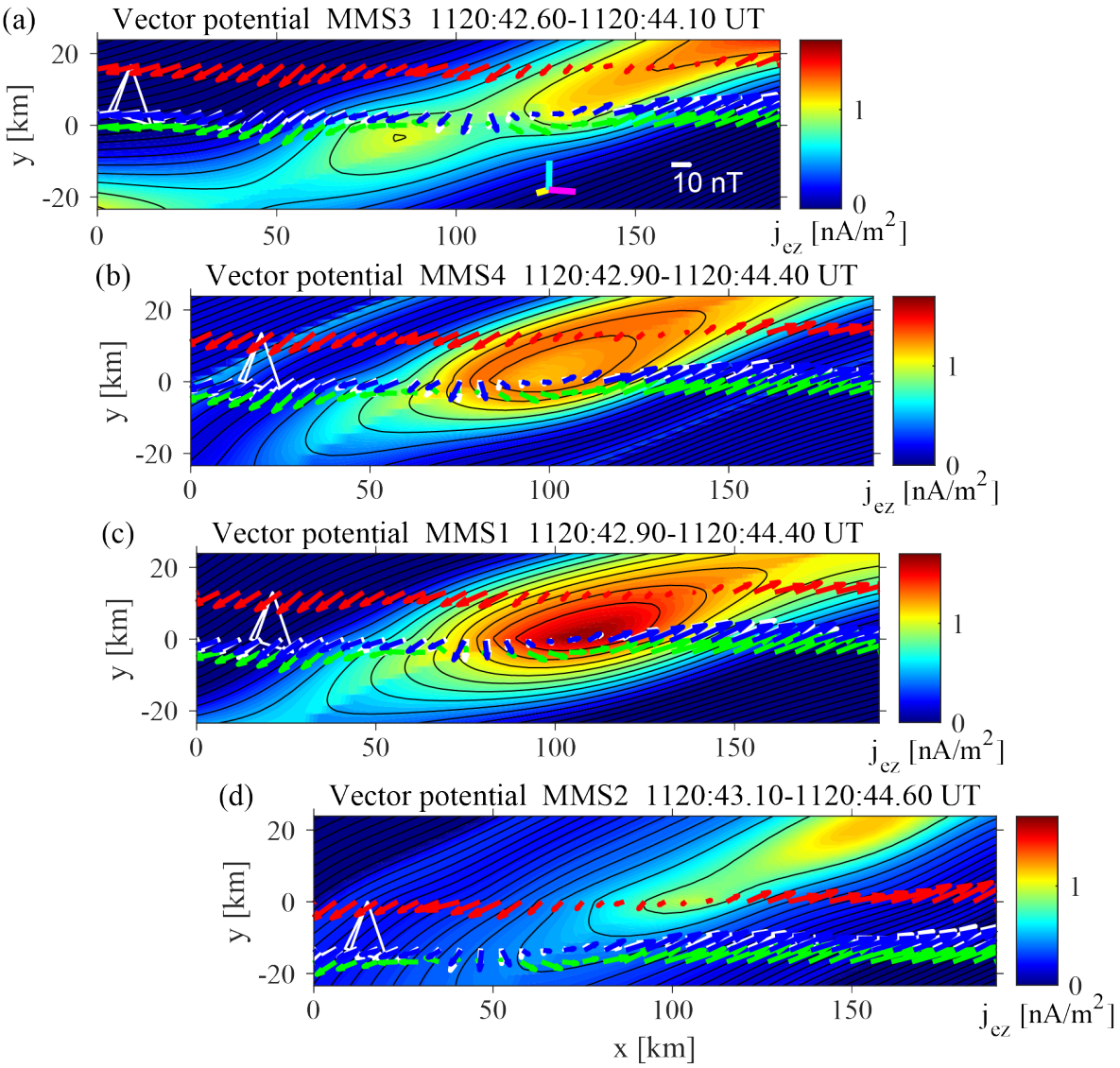

Figure 6. Magnetic field maps from the EMHD reconstruction applied individually to MMS3, MMS4, MMS1, and MMS2 data, respectively, shown in the order of current sheet crossing (Figure 3a). The format of each panel is the same as of Figure 4a. The panels for later crossings are shifted to the right, considering the different crossing times and reconstructed intervals (Figure 3a).

4 Discussion

4.1 Three-dimensional effects

While the reconstruction and MDDB results suggest that the local magnetic

structure in the ECS was roughly 2D, the observed ion-scale flux rope (ISFR) shows features inconsistent with expectations from 2D simulations (Nakamura et al., 2021) or 3D simulation with periodic boundary (Chen et al., 2012) of ISFRs, as will be discussed below. These simulations show that the electron density has a peak at the center of ISFRs, thus the electric field is intense around and points toward the ISFR center (Chen et al., 2012), and the electron temperature is strongly enhanced around the ISFR center, in particular in the parallel direction (Nakamura et al., 2021).

Figure 4e shows the measured parallel electron temperatures plotted along the paths of the four spacecraft (see Figure S3 to clearly see the temperature seen by MMS1), and Figure 7 shows data from various instruments, including the electric field probes, taken by MMS4 around the ISFR interval (the interval 1120:42.8–1120:44.4 UT shown in Figure 7 is nearly the same as that used in the EMHD reconstruction, as shown in Figures 4 and 6b). Whereas the parallel temperature is enhanced around the ISFR boundary, it has a local minimum around the ISFR center (Figure 4e and ~43.6 s in Figure 7e). Moreover, the electron density shows no clear peak (Figure 7b), and the electric field is not intense (Figures 7h and 7i) around the ISFR center. Figure 7d shows that electrons at 0.2-2 keV energies (heated or accelerated electrons of magnetosheath origin) around the ISFR boundaries (~43.4 s and ~43.8 s) were bi-directional with more intense fluxes at pitch angles 0° and 180°. This is consistent with field-line connection to two X-lines and thus magnetic flux rope interpretation. On the other hand, 0.2-2 keV electrons had intense fluxes only at 180° around the ISFR center, suggesting connection to only one X-line. This is contrary to expectation from a 2D flux rope picture. Similar electron pitch-angle distribution signatures have been observed in magnetopause flux ropes (Øieroset et al., 2011; Pu et al., 2013; Zhong et al., 2013), indicating complex magnetic topology of FTEs. These features indicate that the observed ISFR had 3D effects and was not as simple as seen in 2D simulations (Daughton et al., 2006; Drake et al., 2006; Hesse et al., 1999; Nakamura et al., 2021).

The magnetosheath-side separatrix appears to have been encountered by MMS4 at ~43.15 s, after which the parallel temperature increased (Figure 7e), antiparallel streaming electrons were observed throughout, and positive v_{eL} was observed (Figures 4b and 7f) (until ~43.5 s, which was slightly before the ECS center was crossed). Note that in Figure 4b the direction of spacecraft motion and **L** are in the positive x direction. We interpret this positive v_{eL} as electron inflow on the magnetosheath side toward the primary X-line that would have been continuously active and longer than ion scales on the northern side of MMS. This interpretation is consistent with exclusively southward ion jets not only during the FTE intervals but even after the ECS crossing and also with duskward ion flow on the magnetospheric side (Figure 1b), which is expected on the southern side of X-line under duskward magnetosheath field conditions (Figure 8b).

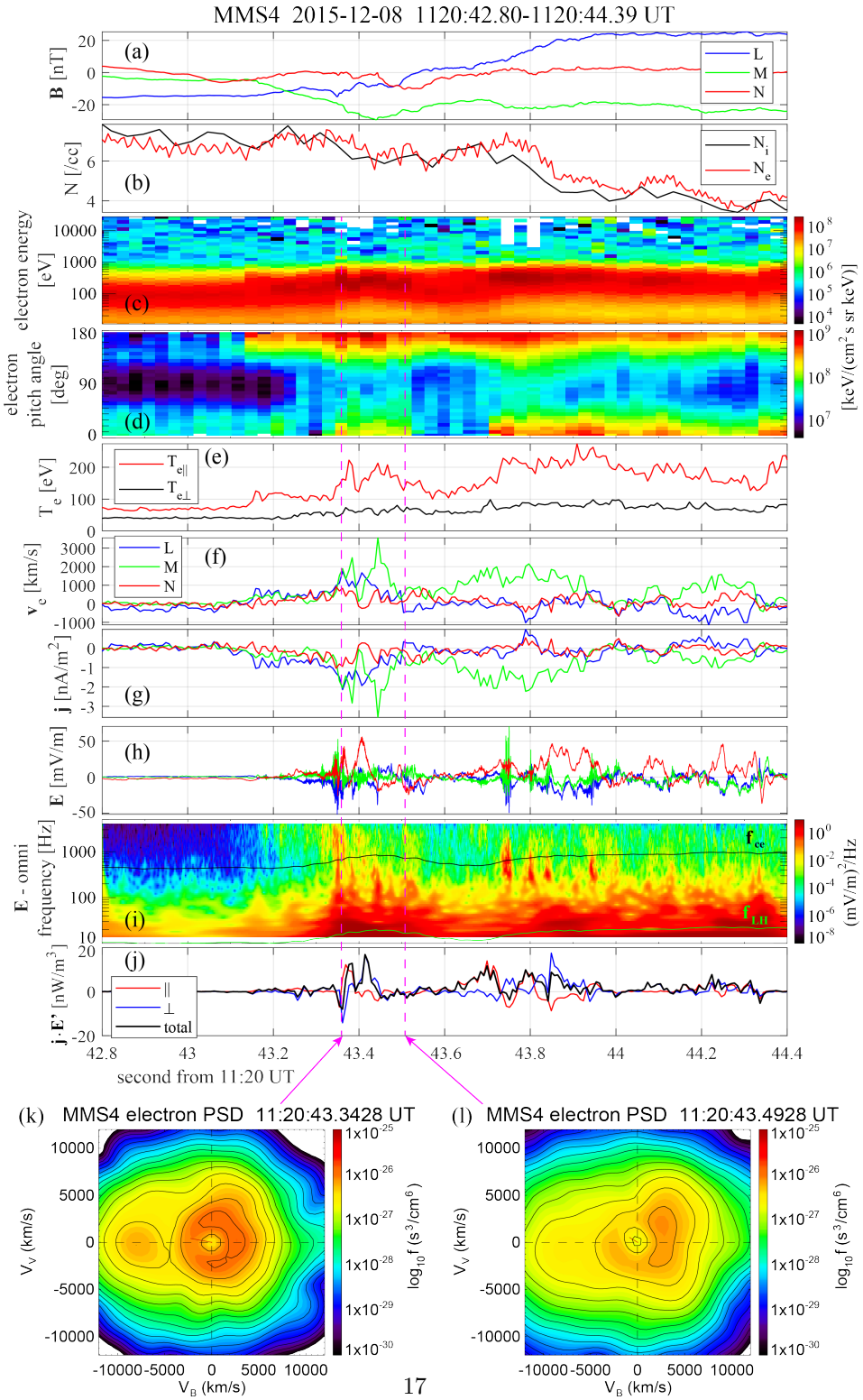
MMS4 2015-12-08 1120:42.80-1120:44.39 UT
(a)
B [nT]
L
M
N
(b)
N [/cc]
N_i
N_e
(c)
electron energy [eV]
[keV/(cm^2 s sr keV)]
(d)
electron pitch angle [deg]
(e)
T_e [eV]
T_e||
T_e⊥
(f)
v_e [km/s]
(g)
j [nA/m^2]
(h)
E [mV/m]
(i)
E - omni frequency [Hz]
f_ce
f_LH
(mV/m)^2/Hz
(j)
j·E' [nW/m^3]
||
⊥
total
second from 11:20 UT
(k) MMS4 electron PSD 11:20:43.3428 UT
(l) MMS4 electron PSD 11:20:43.4928 UT
V_V (km/s)
V_B (km/s)
log10 f (s^3/cm^6)

Figure 7. Burst-mode MMS4 data around the reconstructed ion-scale flux rope (Figure 4). (**a**) Magnetic field in LMN coordinates used in the reconstruction, (**b**) ion and electron densities with 37.5 ms and 7.5 ms resolutions, respectively, (**c**) energy versus time spectrogram of omnidirectional electrons, (**d**) pitch-angle distributions of electrons with energies 0.2–2 keV, (**e**) electron temperatures parallel and perpendicular to the magnetic field, (**f**) electron velocity, (**g**) particle current density, (**h**) electric field data with 8.2 kHz resolution, (**i**) Wavelet power spectrogram of the electric field, and (**j**) parallel and perpendicular component contributions to the electron-frame energy conversion rate $\mathbf{j} \bullet \mathbf{E}'$ and total magnitude with 7.5 ms resolution. The black and green curves in panel (**i**) mark the electron cyclotron and lower-hybrid frequencies ($f_{\rm ce}$ and $f_{\rm LH}$, respectively). (**k,l**) Electron velocity distributions in the BV plane with field-aligned velocity as the horizontal axis and perpendicular velocity as the vertical axis, at times marked by the magenta dashed lines. Electron energy-time spectrogram (**c**), pitch-angle distribution (**d**), electric field power spectrum (**i**), and electron velocity distributions (**k,l**) were created by SPEDAS (Angelopoulos et al., 2019), whereas the other panels by Matlab.

Figures 7k and 7l show examples of electron velocity distributions with bidirectional streaming signatures observed on the magnetosheath side. We interpret anti-field-aligned streaming electrons, observed continuously on the magnetosheath side of the ECS center but on the earthward side of the magnetosheath separatrix (Figure 7d), as those inflowing toward the primary X-line on the northern side of MMS ("aP" on field line "S2" in Figure 8b). Field-aligned electrons, observed only transiently on the magnetosheath side, would be those streaming toward southern, secondary X-line ("pS" on field line "S2"). Asymmetries in speed and phase space density between the field-aligned and anti-field-aligned electrons are likely to be guide-field effects; in the present event, the guide field intensity ~20 nT was comparable to that of the reconnecting field (Figure 3). In the presence of guide field with negative B_M (Figures 7a and 8b), electrons streaming antiparallel to the magnetic field (that is, roughly in the direction antiparallel to the reconnection electric field which is in the $-\mathbf{M}$ direction) are more strongly sucked into the primary reconnection region, producing a density minimum, and are more strongly accelerated than parallel streaming electrons (Pritchett & Coroniti, 2004). Hall magnetic field signature (negative increase of B_M in Figure 7a) and density dip, which is not very clear in Figure 7b but is obvious for MMS2 and MMS3 (Figures S5b and S6b), support our interpretation. Note that a density dip is a signature of magnetosheath-side separatrix regions for asymmetric, guide-field reconnection (Fig. 1 in Choi et al., 2022).

We also note that temporal variations around the ISFR center of the electron temperature and pitch-angle distribution seen by MMS1, which was 14.2 km ($\sim 6d_e$) away from MMS4 in $z_{\rm EMHD}$ (Table S1), differed significantly from those seen by MMS4. Comparison between Figures 7 and S4 suggests that around the ISFR center, MMS4 more often encountered a type "S3" field line, with only anti-field-aligned magnetosheath electrons, while MMS1 more often encountered

a type "S4" field line with bidirectional electrons (see Figure 8b for types of field line). This is consistent with electron-scale 3D structures in the ISFR axial or X-line direction.

These features suggest that the primary X-line on the northern side of MMS was persistently active, but secondary X-line that contributed to the formation of the 3D ISFR in the ECS was patchy or transiently active (Figure 8b). The secondary X-line(s) could have been of sub-ion scale, because no northward ion jet or acceleration was observed (Figure 1b). Figure 8a shows 3D representation of the 2D magnetic field lines from the EMHD reconstruction for MMS4 (Figure 4). One can expect that under significant guide field conditions, as in the present case, field lines may be connected to distant regions where reconnection may or may not be active. The suggested patchy or transient X-line(s) on the sub-ion scale is consistent with 3D fully kinetic simulations of magnetic reconnection with guide field, as reported by Daughton et al. (2011) and Nakamura et al. (2016), in which turbulent reconnection generates 3D filamentary ion-scale flux ropes. On the other hand, turbulent fluctuations of the upstream magnetosheath magnetic field may also have led to the localized and/or intermittent nature of secondary X-line(s) (Genestreti et al., 2022).

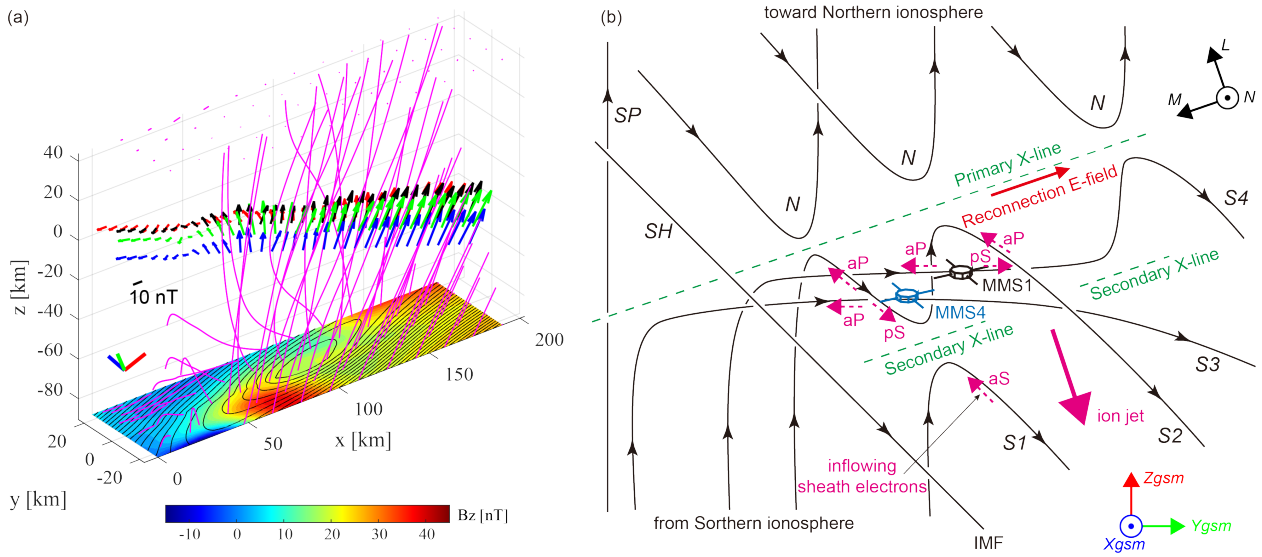

Figure 8. (**a**) Three-dimensional view in reconstruction coordinates of the 2D magnetic field lines recovered from the EMHD reconstruction applied to MMS4 data (Figure 4). The black, red, green, and blue arrows are the vectors of magnetic fields measured by MMS1, MMS2, MMS3, and MMS4, respectively. The blue, green, and red bars at lower left are the unit vectors of the GSM x, y, and z axes, respectively. (**b**) Schematic of possible magnetic topology and geometry of the ion-scale flux rope (ISFR) on the subsolar magnetopause, as viewed from the sun, when MMS4 and MMS1 were near the center of the ISFR.

"SH" and "SP" mark unreconnected magnetosheath and magnetospheric field lines, respectively. "N" marks standard reconnected field lines on the northern side of the primary X-line with connection to the northern ionosphere. "S1" and "S2" mark the field lines formed through reconnection at secondary X-line between two standard reconnected field lines on the southern side of the primary X-line. While "S1" was on the southern side of secondary X-line, "S2" passed through the region inside, but near the boundary of, the ISFR. "S3" is the field line that experienced reconnection at the primary X-line and passed through the central region of the ISFR, and "S4" is the field line that experienced reconnection at both the primary and secondary X-lines and passed through the ISFR central region. Magenta dashed arrows indicate magnetosheath electron populations inflowing toward either primary or secondary X-lines, with "aP" and "aS" representing electrons streaming antiparallel to the magnetic field toward the Primary and Secondary X-lines, respectively, and "pS" the electrons streaming parallel to the field toward Secondary X-line.

4.2 Origin of positive and negative $\mathbf{j} \bullet (\mathbf{E}+\mathbf{v}_e \times \mathbf{B})$

Figure 4d shows the electron-frame energy conversion rate $\mathbf{j} \bullet \mathbf{E}' = \mathbf{j} \bullet (\mathbf{E}+\mathbf{v}_e \times \mathbf{B})$ plotted along the paths of the four spacecraft. As reported by Burch et al. (2018), both positive and negative $\mathbf{j} \bullet \mathbf{E}'$ were observed, indicating that electromagnetic energy was being converted to electron energy in some parts of the ECS and vice versa in other parts. An interesting feature is that many energy conversion regions were distributed in separatrix regions of the ISFR and on both magnetosheath and magnetospheric sides. Note that the magnitude of the energy conversion rates is much larger ($\geq$ 10 nW/m^3) than predicted ($\leq$ 4 nW/m^3) in the EDRs of magnetopause reconnection, as pointed out by Burch et al. (2018), and those energy conversion regions appear far from X-line(s) (Figures 4d and S3d).

Figures 7d, 7e, 7h, and 7j (see also Figures S4-S6 in Supporting Information for the spacecraft other than MMS4) show that many of the large amplitude $\mathbf{j} \bullet \mathbf{E}'$ regions are collocated with large amplitude electric fields and high parallel electron temperature associated with bi-directional field-aligned electrons. The large amplitude electric fields were mostly of electrostatic fluctuations with frequencies below, around, or above the electron cyclotron frequency f_{ce}, many with broadband features (Figure 7i). Burch et al. (2018) reported that some fluctuations observed around the magnetosheath separatrix were of oblique weakly electromagnetic whistler waves with frequencies around f_{ce} (their Figure 3). While the generation mechanisms of these intermediate-frequency waves (Khotyaintsev et al., 2019) are beyond the scope of the present paper and need further investigation, it is probable that they were driven by bi-directional electron beams (Wang et al., 2022), as shown in Figures 7k and 7l. A number of simulations and observations have shown that electron beam-driven or two-stream instabilities and resulting electrostatic waves (EWs), electrostatic solitary waves (ESWs or electron holes), or whistler waves can be responsible for electrostatic and electromagnetic fluctuations around f_{ce} in separatrix regions (Fujimoto, 2014;

Goldman et al., 2014; Holmes et al., 2019; Steinvall et al., 2019; Choi et al., 2022).

Figure 7j (see also Figures S4-S6) shows that the parallel component contribution to $\mathbf{j} \bullet \mathbf{E}^{'}$, $j_{\parallel}E_{\parallel}$, was positive in some regions and negative in other regions. Some intense positive $j_{\parallel}E_{\parallel}$ (e.g., at ~43.37 s) was observed without much electric field fluctuations, and thus may be due to field-aligned (electrostatic potential) acceleration of electrons inflowing toward the primary X-line (Egedal et al., 2015). Other positive $j_{\parallel}E_{\parallel}$ (e.g., at ~43.8 s and ~43.95 s) coexist with intermediate-frequency electrostatic fluctuations, and may be associated with electrostatic wave to electron energy conversion, namely, electron heating. Interestingly, some intense negative $j_{\parallel}E_{\parallel}$ (at ~43.75 s and ~43.83 s in Figure 7j) coexisted with intermediate-frequency electrostatic fluctuations, and may be an indication of electron beam energy being converted to energy of EWs or ESWs.

An intense positive $j_{\parallel}E_{\parallel}$ was seen by MMS4 at ~43.7 s, when no prominent intermediate-frequency electric field fluctuations were observed (Figures 7h-7j). This is possibly associated with energy conversion of actual magnetopause reconnection in the presence of guide field. However, its magnitude (~10 nW/m^3) was much larger than expected for standard magnetopause reconnection (Burch et al., 2018), and it was seen near the ISFR center (Figure 4d) that may have been connected to a portion of the primary X-line (Figure 8). We also note that such intense $\mathbf{j} \bullet \mathbf{E}^{'}$ was not seen by MMS1 near the ISFR center (Figure S4d). Thus, it might be a signature of patchy or bursty reconnection (Genestreti et al., 2022). Moreover, intense positive and negative $\mathbf{j}_{\perp} \bullet \mathbf{E}^{'}_{\perp}$ were seen at ~43.4 s and ~43.84 s with no significant intermediate frequency waves. Since they were observed in density gradient regions, it is possible that they were associated with lower-hybrid waves excited around the separatrices (Pritchett, 2013; Marshall et al., 2022). Further investigation of these features is necessary.

A unique feature of the present event is that both bi-directional electron beams and large-amplitude electric field fluctuations were observed not only in the magnetospheric but also in the magnetosheath separatrix regions, while EWs and ESWs themselves have been observed on the magnetosheath side of magnetopause reconnection layers (Graham et al., 2015, 2016; Zhong, Graham et al., 2021). This would be because of the presence of ISFR with connection to two X-lines. Note that those in magnetospheric separatrix regions are common (Hwang et al., 2017; Wilder et al., 2017, 2019; Khotyaintsev et al., 2020), and this is attributed partially to higher speeds on the magnetospheric side of magnetosheath-origin electrons as they are accelerated in the EDR by the reconnection electric field before entering into magnetospheric separatrix regions (in addition to acceleration in magnetosheath separatrix regions) (e.g., Choi et al., 2022).

In summary, the origin of oscillatory or positive and negative localized $\mathbf{j} \bullet \mathbf{E}^{'}$ appears to be in the separatrix regions, associated with intermediate-frequency waves (EWs, ESWs, or double layers) generated by bi-directional electron beams or lower-hybrid waves excited in density gradient regions (Graham et al., 2019;

Marshall et al., 2022). It is also possible that 3D or transient nature of magnetopause reconnection in the presence of guide field (Daughton et al., 2011) or magnetosheath turbulence (Genestreti et al., 2022), as discussed in section 4.1, was responsible for them. The results suggest that while intense $\mathbf{j} \bullet \mathbf{E}'$ can be used as an indicator of active reconnection not far from the observation site, it may not necessarily indicate electron-scale proximity to EDRs of major magnetic topology change. Note, however, that the field-line connectivity can change in double layer-like structures (Schindler et al., 1988), which can exist in separatrix regions and may exhibit intense $j_{\parallel}E_{\parallel} > 0$ features (Ergun et al., 2016).

4.3 Generation and decay processes of flux transfer events

We argue that the three FTEs or FRs preceding the magnetopause ECS were produced by the same mechanism that generated the ISFR in the ECS, namely, secondary reconnection. Table 1 shows the HT velocity, which can be taken as the FTE structure velocity, the axial orientations of the three FRs, and their angles relative to the ISFR axis. It is seen that the FR2 and FR3 axes were relatively close to the ISFR axis, and the southward component of the HT velocity was larger for FR3, closest to the reconnecting ECS, than for FR1. These results are consistent with FTE generation near the primary X-line that formed the ISFR, and suggest that the FTEs initially had higher speeds near the X-line but were decelerated as they traveled southward and plowed through ambient plasmas. Thus, our analysis supports the conclusion by Dong et al. (2017) that FTEs can form through secondary magnetic reconnection in elongated electron-scale current sheets (Daughton et al., 2006; Drake et al., 2006). The FR1 axial direction is rather different. This is likely because FR1 was observed not near the current sheet center but in the magnetosheath (Figure 1a). Note that the single-spacecraft method for FR axis estimation (Hu and Sonnerup, 2002) tends to give axial orientations closer to the average magnetic field direction for the reconstruction interval, that is the period when an FTE or FR is encountered.

Our study suggests that ion-scale flux ropes and meso-scale FTEs (on ion-to-MHD scales smaller than typical FTEs with sizes ~1 R_E) (Hasegawa et al., 2016) can be generated from electron-scale current sheets with single primary X-line but with secondary X-line(s). However, we do not claim that all FTEs can be generated by the same mechanism, that is, from single primary X-line. There are at least two types of magnetopause FRs or FTEs: one type embedded in unidirectional reconnection ion jets, and the other sandwiched between oppositely directed, colliding reconnection ion jets. The former type is those seen in Figure 1 and as reported by Phan et al. (2004) and Hasegawa et al. (2016) that appear to be observed during continuous magnetopause reconnection. The latter type was reported by Hasegawa et al. (2010) and Øieroset et al. (2011) and may require more than one X-lines with MHD-scale separation from each other (otherwise no colliding ion jets) or sequential formation of primary X-lines (Raeder, 2006). There may also be FTEs formed through intermittent bursts of magnetopause reconnection at single X-line (Fear et al., 2012).

Hasegawa et al. (2016) suggested, based on simultaneous Geotail and MMS observations of reconnection jets at the dayside magnetopause at low- and mid-latitudes, respectively, that meso-scale FTEs may decay during the course of poleward propagation. As reported recently by Øieroset et al. (2016, 2019), Kacem et al. (2018), Fargette et al. (2020), Qi et al. (2020), and Zhong, Zhou et al. (2021), magnetic flux tubes and energy in meso-scale or ion-scale FRs may be disentangled and dissipated, respectively, by magnetic reconnection inside or at the boundary of FTEs. These FTE decay processes may contribute to the formation of the low-latitude boundary layer (Nishida, 1989) and a collection of such processes may affect dayside to nightside flux transfer on the large scale. Thus, further exploration is needed of FTE evolution processes.

5 Summary

We have analyzed three flux transfer events (FTEs) and a subsequent electron-scale magnetopause current sheet (ECS), which was reconnecting in the presence of significant guide field and showed intense positive and negative values of $\mathbf{j} \bullet \mathbf{E}^{'}$, observed by the MMS spacecraft on 8 December 2015. The results can be summarized as follows.

1. The reconstructions of the ECS by both the EMHD and polynomial reconstruction methods suggest that an ion-scale magnetic flux rope (ISFR) existed and was likely growing in the ECS, consistent with ISFR generation by secondary magnetic reconnection.

2. Grad-Shafranov reconstruction shows that the axial orientations of two of the three FTE flux ropes that were closer to the ECS than the other were similar to that of the ISFR, suggesting the same generation mechanism, that is, secondary reconnection in ECS.

3. While bi-directional electron beams observed in separatrix regions of the ISFR are consistent with X-lines on both the northern and southern sides of the ISFR, unidirectional electrons consistent with connection to only the northern X-line were observed around the ISFR center. This suggests three-dimensional magnetic topology of the observed ISFR. The localized or transient nature of intense $\mathbf{j} \bullet \mathbf{E}^{'} > 0$ around the ISFR center, seen by MMS4 but not by other spacecraft, is consistent with such interpretation. It is likely that secondary reconnection in the present event with significant guide field was patchy or intermittent.

4. Most of intense oscillatory energy conversion features were observed in separatrix regions of the ISFR, many collocated with bi-directional electron beams and/or large-amplitude electric field fluctuations suggestive of electrostatic waves or structures (solitary waves or double layers). In the present event, intense $\mathbf{j} \bullet \mathbf{E}^{'}$ appears to be mostly due to activities in the separatrix regions, rather than to energy conversion in the EDR.

5. The last point implies that while significant $\mathbf{j} \bullet \mathbf{E}^{'}$ may be an indication of active reconnection site not far from the observation site, it may not

necessarily indicate close (electron-scale) vicinity to region(s) of major magnetic topology change. Spacecraft measurements with multi-scale separations would be needed to reveal time history of multi-dimensional and cross-scale energy conversion and transfer phenomena and effects of the upstream and asymmetric boundary conditions (Genestreti et al., 2022).

A final remark is that while the present EMHD reconstruction assumes isotropy of the gyrotropic part of electron velocity distributions (Hasegawa et al., 2021), strong electron temperature anisotropy is common in reconnection layers (Figures 1e and 7e), in particular, in the presence of guide field (e.g., Wetherton et al., 2022). Further improvement of the EMHD method is thus necessary to incorporate electron pressure anisotropy effects.

Acknowledgments

The work by H.H. was supported by JSPS Grant-in-aid for Scientific Research KAKENHI 21K03504. Part of the work done while H.H. was at SwRI was supported by NASA Contract No. NNG04EB99C at SwRI. R.E.D was supported by a NASA grant (80NSSC22K1109). T.K.M.N. was supported by the Austrian Research Fund (FWF) P32175-N27.

Open Research

All MMS data used in this study are publicly available via the MMS Science Data Center at https://lasp.colorado.edu/mms/sdc/public/about/browse-wrapper/. All code used to produce the MMS data analyzed in this study is based on the publicly available SPEDAS tools (Angelopoulos et al., 2019) (http://spedas.org/downloads/spedas_5_0.zip). The Matlab code for the EMHD reconstruction can be found at the Zenodo (https://doi.org/10.5281/zenodo.5144478), while that for the Grad-Shafranov reconstruction is available at GitHub (https://github.com/cmoestl/interplanetary-grad-shafranov). The Matlab code for polynomial reconstruction using data from multiple times, used for producing Figure S2, is available in a Zenodo repository (https://doi.org/10.5281/zenodo.6941597).

References

Angelopoulos, V., Cruce, P., Drozdov, A., et al. (2019). The Space Physics Environment Data Analysis System (SPEDAS). *Space Sci. Rev.*, *215*, 9. https://doi.org/10.1007/s11214-018-0576-4.

Burch, J. L., & Phan, T. D. (2016). Magnetic reconnection at the dayside magnetopause: Advances with MMS, *Geophys. Res. Lett.*, *43*, 8327–8338, doi:10.1002/2016GL069787.

Burch, J. L., Torbert, R. B., Phan, T. D., et al. (2016). Electron-scale measurements of magnetic reconnection in space, *Science*, *352*, aaf2939, doi:10.1126/science.aaf2939.

Burch, J. L., Ergun, R. E., Cassak, P. A., Webster, J. M., Torbert, R. B., Giles, B. L., et al. (2018), Localized oscillatory energy conversion in magnetopause

reconnection. *Geophysical Research Letters*, *45*, 1237–1245. https://doi.org/10.1002/2017GL076809.

Burch, J. L., Webster, J. M., Hesse, M., Genestreti, K. J., Denton, R. E., & Phan, T. D., et al. (2020). Electron inflow velocities and reconnection rates at Earth's magnetopause and magnetosheath. *Geophysical Research Letters*, *47*, e2020GL089082. https://doi.org/10.1029/2020GL089082.

Chen, L.-J., Daughton, W., Bhattacharjee, A., Torbert, R. B., Roytershteyn, V., et al. (2012). In-plane electric fields in magnetic islands during collisionless magnetic reconnection, *Phys. Plasmas*, *19*, 112902, doi:10.1063/1.4767645.

Choi, S., Bessho, N., Wang, S., Chen, L.-J., & Hesse, M. (2022). Whistler waves generated by nongyrotropic and gyrotropic electron beams during asymmetric guide field reconnection. *Phys. Plasmas*, *29*, 012903, https://doi.org/10.1063/5.0059884.

Daughton, W., Scudder, J., & Karimabadi, H. (2006). Fully kinetic simulations of undriven magnetic reconnection with open boundary conditions, *Phys. Plasmas*, *13*, 072101, https://doi.org/10.1063/1.2218817.

Daughton, W., V. Roytershteyn, H. Karimabadi, L. Yin, B. J. Albright, B. Bergen, and K. J. Bowers (2011). Role of electron physics in the development of turbulent magnetic reconnection in collisionless plasmas. *Nature Phys.*, *7*, 539–542, doi:10.1038/nphys1965.

Denton, R. E., Sonnerup, B. U. Ö., Russell, C. T., Hasegawa, H., Phan, T.-D., Strangeway, R. J., et al. (2018). Determining L-M-N current sheet coordinates at the magnetopause from Magnetospheric Multiscale data. *Journal of Geophysical Research: Space Physics*, *123*, 2274–2295. https://doi.org/10.1002/2017JA024619.

Denton, R. E., Torbert, R. B., Hasegawa, H., Dors, I., Genestreti, K. J., Argall, M. R., et al. (2020). Polynomial reconstruction of the reconnection magnetic field observed by multiple spacecraft. *Journal of Geophysical Research: Space Physics*, *125*, e2019JA027481. https://doi.org/10.1029/2019JA027481.

Denton, R. E., Liu, Y.-H., Hasegawa, H., Torbert, R. B., Li, W., Fuselier, S., & Burch, J. L. (2022). Polynomial reconstruction of the magnetic field observed by multiple spacecraft with integrated velocity determination. *Journal of Geophysical Research: Space Physics*, *127*, e2022JA030512. https://doi.org/10.1029/2022JA030512.

Dong, X.-C., Dunlop, M. W., Trattner, K. J., et al. (2017). Structure and evolution of flux transfer events near dayside magnetic reconnection dissipation region: MMS observations, *Geophys. Res. Lett.*, *44*, 5951–5959, doi:10.1002/2017GL073411.

Drake, J. F., Swisdak, M., Schoeffler, K. M., Rogers, B. N., & Kobayashi, S. (2006). Formation of secondary islands during magnetic reconnection, *Geophys. Res. Lett.*, *33*, L13105, doi:10.1029/2006GL025957.

Eastwood, J. P., Phan, T. D., Cassak, P. A., et al. (2016). Ion-scale secondary flux ropes generated by magnetopause reconnection as resolved by MMS, *Geophys. Res. Lett.*, *43*, 4716–4724, doi:10.1002/2016GL068747.

Egedal, J., Daughton, W., Le, A., & Borg, A. L. (2015). Double layer electric fields aiding the production of energetic flat-top distributions and superthermal electrons within magnetic reconnection exhausts, *Phys. Plasmas*, *22*, 101208, doi:10.1063/1.4933055.

Ergun, R. E., Tucker, S., Westfall, J., et al. (2016). The axial double probe and fields signal processing for the MMS mission. *Space Sci. Rev.*, *199*, 167–188. doi:10.1007/s11214-014-0115-x.

Ergun, R. E., K. A. Goodrich, F. D. Wilder, et al. (2016). Magnetospheric Multiscale satellites observations of parallel electric fields associated with magnetic reconnection. *Phys. Rev. Lett.*, *116*, 235102, doi:10.1103/PhysRevLett.116.235102.

Fargette, N., Lavraud, B., Øieroset, M., Phan, T. D., Toledo-Redondo, S., Kieokaew, R., et al. (2020). On the ubiquity of magnetic reconnection inside flux transfer event-like structures at the Earth's magnetopause. *Geophysical Research Letters*, *47*, e2019GL086726. https://doi.org/10.1029/2019GL086726.

Fear, R. C., Milan, S. E., & Oksavik, K. (2012). Determining the axial direction of high-shear flux transfer events: Implications for models of FTE structure. *J. Geophys. Res.*, *117*, A09220. doi:10.1029/2012JA017831.

Fujimoto, K. (2014). Wave activities in separatrix regions of magnetic reconnection, *Geophys. Res. Lett.*, *41*, 2721–2728, https://doi.org/10.1002/2014GL059893.

Genestreti, K. J., Burch, J. L., Cassak, P. A., Torbert, R. B., Ergun, R. E., Varsani, A., ... Allen, R. C. (2017). The effect of a guide field on local energy conversion during asymmetric magnetic reconnection: MMS observations. *Journal of Geophysical Research: Space Physics*, *122*, 11342–11353. https://doi.org/10.1002/2017JA024247.

Genestreti, K. J., Li, X., Liu, Y.-H., et al. (2022). On the origin of "patchy" energy conversion in electron diffusion regions. *Phys. Plasmas*, *29*, 082107, https://doi.org/10.1063/5.0090275.

Goldman, M. V., Newman, D. L., Lapenta, G., et al. (2014). Cerenkov emission of quasiparallel whistlers by fast electron phase-space holes during magnetic reconnection, *Phys. Rev. Lett.*, *112*, 145002, https://doi.org/10.1103/PhysRevLett.112.145002.

Graham, D. B., Khotyaintsev, Y. V., Vaivads, A., & Andre, M. (2015). Electrostatic solitary waves with distinct speeds associated with asymmetric reconnection, *Geophys. Res. Lett.*, *42*, 215–224, doi:10.1002/2014GL062538.

Graham, D. B., Khotyaintsev, Y. V., Vaivads, A., & Andre, M. (2016). Electrostatic solitary waves and electrostatic waves at the magnetopause, *J. Geophys. Res. Space Physics*, *121*, 3069–3092, doi:10.1002/2015JA021527.

Graham, D. B., Khotyaintsev, Yu. V., Norgren, C., Vaivads, A., Andre, M., Drake, J. F., et al. (2019). Universality of lower hybrid waves at Earth's magnetopause. *J. Geophys. Res. Space Physics*, *124*, 8727–8760. https://doi.org/10.1029/2019JA027155.

Hasegawa, H. (2012). Structure and dynamics of the magnetopause and its boundary layers, *Monogr. Environ. Earth Planets*, *1*(2), 71–119, doi:10.5047/meep.2012.00102.0071.

Hasegawa, H., Sonnerup, B. U. Ö., Owen, C. J., Klecker, B., Paschmann, G., Balogh, A., & Rème, H. (2006). The structure of flux transfer events recovered from Cluster data, *Ann. Geophys.*, *24*, 603–618, doi:10.5194/angeo-24-603-2006.

Hasegawa, H., Wang, J., Dunlop, M. W., Pu, Z. Y., Zhang, Q.-H., et al. (2010). Evidence for a flux transfer event generated by multiple X-line reconnection at the magnetopause, *Geophys. Res. Lett.*, *37*, L16101, doi:10.1029/2010GL044219.

Hasegawa, H., Sonnerup, B. U. Ö., Eriksson, S., Nakamura, T. K. M., & Kawano, H. (2015). Dual-spacecraft reconstruction of a three-dimensional magnetic flux rope at the Earth's magnetopause, *Ann. Geophys.*, *33*, 169–184, doi:10.5194/angeo-33-169-2015.

Hasegawa, H., Kitamura, N., Saito, Y., Nagai, T., Shinohara, I., et al. (2016). Decay of mesoscale flux transfer events during quasi-continuous spatially extended reconnection at the magnetopause, *Geophys. Res. Lett.*, *43*, 4755–4762, doi:10.1002/2016GL069225.

Hasegawa, H., Sonnerup, B. U. Ö., Denton, R. E., et al. (2017). Reconstruction of the electron diffusion region observed by the Magnetospheric Multiscale spacecraft: First results, *Geophys. Res. Lett.*, *44*, 4566–4574, doi:10.1002/2017GL073163.

Hasegawa, H., Nakamura, T. K. M., & Denton, R. E. (2021). Reconstruction of the electron diffusion region with inertia and compressibility effects. *Journal of Geophysical Research: Space Physics*, *126*, e2021JA029841. https://doi.org/10.1029/2021JA029841.

Hasegawa, H., Denton, R. E., Nakamura, T. K. M., Genestreti, K. J., Phan, T. D., Nakamura, R., et al. (2022). Magnetic Field Annihilation in a Magnetotail Electron Diffusion Region with Electron-scale Magnetic Island. *Journal of Geophysical Research: Space Physics*, *127*, e2022JA030408. https://doi.org/10.1029/2022JA030408.

Hau, L.-N., & Sonnerup, B. U. Ö. (1999). Two-dimensional coherent structures in the magnetopause: Recovery of static equilibria from single-spacecraft data, *J. Geophys. Res.*, *104*(A4), 6899–6917, doi:10.1029/1999JA900002.

Hesse, M., Schindler, K., Birn, J., & Kuznetsova, M. (1999). The diffusion region in collisionless magnetic reconnection, *Phys. Plasmas*, *6*, 1781–1795, https://doi.org/10.1063/1.873436.

Holmes, J. C., Ergun, R. E., Nakamura, R., Roberts, O., Wilder, F. D., & Newman, D. L. (2019). Structure of electron-scale plasma mixing along the dayside reconnection separatrix. *Journal of Geophysical Research: Space Physics*, *124*, 8788-8803. https://doi.org/10.1029/2019JA026974.

Hu, Q., & Sonnerup, B. U. Ö. (2002). Reconstruction of magnetic clouds in the solar wind: Orientations and configurations, *J. Geophys. Res.*, *107*(A7), doi:10.1029/2001JA000293.

Hu, Q., & Sonnerup, B. U. Ö. (2003). Reconstruction of two-dimensional structures in the magnetopause: Method improvements, *J. Geophys. Res.*, *108*(A1), 1011, doi:10.1029/2002JA009323.

Hwang, K.-J., Sibeck, D. G., Choi, E., et al. (2017). Magnetospheric Multiscale mission observations of the outer electron diffusion region, *Geophys. Res. Lett.*, *44*, 2049–2059, doi:10.1002/2017GL072830.

Kacem, I., Jacquey, C., Genot, V., Lavraud, B., Vernisse, Y., Marchaudon, A., et al. (2018). Magnetic reconnection at a thin current sheet separating two interlaced flux tubes at the Earth's magnetopause. *Journal of Geophysical Research: Space Physics*, *123*, 1779–1793, https://doi.org/10.1002/2017JA024537.

Khotyaintsev, Y. V., Graham, D. B., Norgren, C., & Vaivads, A. (2019). Collisionless Magnetic Reconnection and Waves: Progress Review. *Front. Astron. Space Sci.*, *6*, 70. doi:10.3389/fspas.2019.00070.

Khotyaintsev, Y. V., Graham, D. B., Steinvall, K., et al. (2020). Electron heating by Debye-scale turbulence in guide-field reconnection. *Phys. Rev. Lett.*, *124*, 045101. https://doi.org/10.1103/PhysRevLett.124.045101.

Khrabrov, A. V., & Sonnerup, B. U. Ö. (1998). DeHoffmann-Teller Analysis, in *Analysis Methods for Multi-Spacecraft Data*, edited by G. Paschmann and P. W. Daly, chap. 9, pp.221–248, Int. Space Sci. Inst., Bern, Switzerland, and Eur. Space Agency, Paris, France.

Lindqvist, P.-A., Olsson, G., Torbert, R. B., et al. (2016). The Spin-plane Double Probe electric field instrument for MMS. *Space Sci. Rev.*, *199*, 137–165. doi:10.1007/s11214-014-0116-9.

Liu, Y.-H., Hesse, M., Guo, F., Daughton, W., Li, H., Cassak, P. A., & Shay, M. A. (2017). Why does steady-state magnetic reconnection have a maximum local rate of order 0.1? *Phys. Rev. Lett.*, *118*, 085101, doi:10.1103/PhysRevLett.118.085101.

Marshall, A. T., Burch, J. L., Reiff, P. H., Webster, J. M., Denton, R. E., Rastaetter, L., Torbert, R. B., Ergun, R. E., Russell, C. T., and Gershman, D.

J. (2022). Lower hybrid drift wave motion at a dayside magnetopause x-line with energy conversion dominated by a parallel electric field, *Phys. Plasmas*, *29*, 012905, https://doi.org/10.1063/5.0071159.

Nakamura, T. K. M., Nakamura, R., Narita, Y., Baumjohann, W., & Daughton, W. (2016). Multi-scale structures of turbulent magnetic reconnection, *Phys. Plasmas*, *23*, 052116, doi:10.1063/1.4951025.

Nakamura, T. K. M., Hasegawa, H., Genestreti, K. J., Denton, R. E., Phan, T. D., Stawarz, J. E., et al. (2021). Fast cross-scale energy transfer during turbulent magnetic reconnection. *Geophysical Research Letters*, *48*, e2021GL093524. https://doi.org/10.1029/2021GL093524.

Nishida, A. (1989). Can random reconnection on the magnetopause produce the low latitude boundary layer? *Geophys. Res. Lett.*, *16*, 227–230.

Øieroset, M., Phan, T. D., Eastwood, J. P., Fujimoto, M., Daughton, W., et al. (2011). Direct evidence for a three-dimensional magnetic flux rope flanked by two active magnetic reconnection X lines at Earth's magnetopause, *Phys. Rev. Lett.*, *107*, 165007, doi:10.1103/PhysRevLett.107.165007.

Øieroset, M., Phan, T. D., Drake, J. F., Eastwood, J. P., Fuselier, S. A., Strangeway, R. J., et al. (2019). Reconnection with magnetic flux pileup at the interface of converging jets at the magnetopause. *Geophysical Research Letters*, *46*, 1937–1946. https://doi.org/10.1029/2018GL080994.

Paschmann, G., & Sonnerup, B. U. Ö. (2008). Proper frame determination and Walén test, in *Multi-spacecraft analysis methods revisited*, edited by G. Paschmann and P. W. Daly, ISSI SR-008, pp. 65–74, ESA Publications Division.

Phan, T. D., Dunlop, M. W., Paschmann, G., et al. (2004). Cluster observations of continuous reconnection at the magnetopause under steady interplanetary magnetic field conditions, *Ann. Geophys.*, *22*, 2355–2367. https://doi.org/10.5194/angeo-22-2355-2004.

Pollock, C., Moore, T., Jacques, A., et al. (2016). Fast plasma investigation for Magnetospheric Multiscale. *Space Sci. Rev.*, *199*, 331–406. doi:10.1007/s11214-016-0245-4.

Pritchett, P. L., & Coroniti, F. V. (2004). Three-dimensional collisionless magnetic reconnection in the presence of a guide field, *J. Geophys. Res.*, *109*, A01220, doi:10.1029/2003JA009999.

Pritchett, P. L. (2013). The influence of intense electric fields on three-dimensional asymmetric magnetic reconnection. *Phys. Plasmas*, *20*, 061204. doi:10.1063/1.4811123.

Pu, Z. Y., Raeder, J., Zhong, J., Bogdanova, Y. V., Dunlop, M., Xiao, C. J., Wang, X. G., & Fazakerley, A. (2013). Magnetic topologies of an in vivo FTE observed by Double Star/TC-1 at Earth's magnetopause. *Geophys. Res. Lett.*, *40*, 3502–3506, https://doi.org/10.1002/grl.50714.

Qi, Y., Russell, C. T., Jia, Y.-D., & Hubbert, M. (2020). Temporal Evolution of Flux Tube Entanglement at the Magnetopause as Observed by the MMS Satellites. *Geophysical Research Letters*, *47*, e2020GL090314. https://doi.org/10.1029/2020GL090314.

Raeder, J. (2006). Flux Transfer Events: 1. generation mechanism for strong southward IMF, *Ann. Geophys.*, *24*, 381–392.

Rager, A. C., Dorelli, J. C., Gershman, D. J., Uritsky, V., Avanov, L. A., Torbert, R. B., ... Saito, Y. (2018). Electron crescent distributions as a manifestation of diamagnetic drift in an electron-scale current sheet: Magnetospheric Multiscale observations using new 7.5 ms Fast Plasma Investigation moments. *Geophysical Research Letters*, *45*, 578–584. https://doi.org/10.1002/2017GL076260.

Russell, C. T., Anderson, B. J., Baumjohann, W., et al. (2016). The Magnetospheric Multiscale Magnetometers, *Space Sci. Rev.*, *199*, 189–256. doi:10.1007/s11214-014-0057-3.

Schindler, K., Hesse, M., and Birn, J. (1988). General magnetic reconnection, parallel electric fields, and helicity. *J. Geophys. Res.*, *93*(A6), 5547–5557, doi:10.1029/JA093iA06p05547.

Shi, Q. Q., Shen, C., Pu, Z. Y., Dunlop, M. W., Zong, Q.-G., Zhang, H., Xiao, C. J., Liu, Z. X., & Balogh, A. (2005). Dimensional analysis of observed structures using multipoint magnetic field measurements: Application to Cluster, *Geophys. Res. Lett.*, *32*, L12105, doi:10.1029/2005GL022454.

Shi, Q. Q., Shen, C., Dunlop, M. W., Pu, Z. Y., Zong, Q.-G., Liu, Z.-X., Lucek, E. A., & Balogh, A. (2006). Motion of observed structures calculated from multipoint magnetic field measurements: Application to Cluster, *Geophys. Res. Lett.*, *33*, L08109, doi:10.1029/2005GL025073.

Shi, Q. Q., Tian, A. M., Bai, S. C., Hasegawa, H., Degeling, A. W., Pu, Z. Y., Dunlop, M., Guo, R. L., Yao, S. T., Zong, Q.-G., Wei, Y., Zhou, X.-Z., Fu, S. Y., & Liu, Z. Q. (2019). Dimensionality, coordinate system and reference frame for analysis of in-situ space plasma and field data, *Space Sci. Rev.*, *215*, 35, https://doi.org/10.1007/s11214-019-0601-2.

Sonnerup, B. U. Ö., Hasegawa, H., Teh, W.-L., & Hau, L.-N. (2006). Grad-Shafranov reconstruction: An overview, *J. Geophys. Res. Space Physics*, *111*, A09204, doi:10.1029/2006JA011717.

Sonnerup, B. U. Ö., Hasegawa, H., Denton, R. E., & Nakamura, T. K. M. (2016). Reconstruction of the electron diffusion region, *J. Geophys. Res. Space Physics*, *121*, 4279–4290, doi:10.1002/2016JA022430.

Steinvall, K., Khotyaintsev, Y. V., Graham, D. B., Vaivads, A., Le Contel, O., and Russell, C. T. (2019). Observations of electromagnetic electron holes and evidence of Cherenkov whistler emission, *Phys. Rev. Lett.*, *123*, 255101, https://doi.org/10.1103/PhysRevLett.123.255101.

Stawarz, J. E., Eastwood, J. P., Genestreti, K. J., Nakamura, R., Ergun, R. E., Burgess, D., et al. (2018). Intense electric fields and electron-scale substructure within magnetotail flux ropes as revealed by the Magnetospheric Multiscale mission. *Geophysical Research Letters*, *45*, 8783–8792. https://doi.org/10.1029/2018GL079095.

Torbert, R. B., Dors, I., Argall, M. R., Genestreti, K. J., Burch, J. L., Farrugia, C. J., et al. (2020). A new method of 3-D magnetic field reconstruction. *Geophysical Research Letters*, *47*, e2019GL085542. https://doi.org/10.1029/2019GL085542.

Webster, J. M., Burch, J. L., Reiff, P. H., Daou, A. G., Genestreti, K. J., Graham, D. B., et al. (2018). Magnetospheric Multiscale Dayside Reconnection Electron Diffusion Region Events. *Journal of Geophysical Research: Space Physics*, *123*, 4858-4878, https://doi.org/10.1029/2018JA025245.

Wang, S., Bessho, N., Graham, D. B., Le Contel, O., Wilder, F. D., Khotyaintsev, Y. V., et al. (2022). Whistler waves associated with electron beams in magnetopause reconnection diffusion regions. *Journal of Geophysical Research: Space Physics*, *127*, e2022JA030882. https://doi.org/10.1029/2022JA030882.

Wetherton, B. A., Egedal, J., Le, A., & Daughton, W. (2022). Generation of a strong parallel electric field and embedded electron jet in the exhaust of moderate guide field reconnection. *Geophysical Research Letters*, *49*, e2022GL098907. https://doi.org/10.1029/2022GL098907.

Wilder, F. D., Ergun, R. E., Newman, D. L., et al. (2017). The nonlinear behavior of whistler waves at the reconnecting dayside magnetopause as observed by the Magnetospheric Multiscale mission: A case study, *J. Geophys. Res. Space Physics*, *122*, 5487–5501. doi:10.1002/2017JA024062.

Wilder, F. D., Ergun, R. E., Hoilijoki, S., Webster, J., Argall, M. R., Ahmadi, N., et al. (2019). A survey of plasma waves appearing near dayside magnetopause electron diffusion region events. *Journal of Geophysical Research: Space Physics*, *124*, 7837–7849. https://doi.org/10.1029/2019JA027060.

Zenitani, S., Hesse, M., Klimas, A., & Kuznetsova, M. (2011). New measure of the dissipation region in collisionless magnetic reconnection. *Phys. Rev. Lett.*, *106*, 195003. doi:10.1103/PhysRevLett.106.195003.

Zhong, J., Pu, Z. Y., Dunlop, M. W., et al. (2013). Three-dimensional magnetic flux rope structure formed by multiple sequential X-line reconnection at the magnetopause. *J. Geophys. Res. Space Physics*, *118*, 1904–1911, doi:10.1002/jgra.50281.

Zhong, Z. H., Graham, D. B., Khotyaintsev, Y. V., Zhou, M., Le Contel, O., Tang, R. X., & Deng, X. H. (2021). Whistler and broadband electrostatic waves in the multiple X-line reconnection at the magnetopause. *Geophysical Research Letters*, *48*, e2020GL091320. https://doi.org/10.1029/2020GL091320.

Zhong, Z. H., Zhou, M., Deng, X. H., Song, L. J., Graham, D. B., Tang, R. X., et al. (2021). Three-dimensional electron-scale magnetic reconnection in Earth's magnetosphere. *Geophysical Research Letters*, *48*, e2020GL090946. https://doi.org/10.1029/2020GL090946.